International Journal of Mechanical Sciences 242 (2023) 107974

Contents lists available at ScienceDirect

International Journal of Mechanical Sciences

journal homepage: www.elsevier.com/locate/ijmecsci

An efficient algorithm for critical plane factors evaluation

A. Chiocca [a,b,*], F. Frendo [a], G. Marulo [b]

[a] Department of Civil and Industrial Engineering, University of Pisa, Pisa, Italy
[b] Pierburg Pump Technology Italy S.p.A., Livorno, Italy

ARTICLE INFO

Keywords:
Critical plane approach
Multiaxial fatigue
Uniaxial fatigue
Computational cost
Algorithm efficiency
Finite element analysis

ABSTRACT

Fatigue of structural components is a widely discussed subject on which extensive research is still being carried out, both in the scientific and industrial communities. Fatigue damage still represents a major issue for both metallic and non-metallic components, sometimes leading to unforeseen failures for in-service parts. Among all the assessment methodologies, critical plane methods gained a lot of relevance, as they allow the identification of the component's critical location and the direction of early crack propagation. However, the standard method employed for calculating critical plane factors is very time-consuming as it makes use of nested *for/end* loops and, for that reason, it is usually applied in a research context, or when the critical areas of the component are known. Very often, however, the critical regions cannot be identified, due to complex geometries, loads or constraints, or the fatigue assessment has to be carried out with tight time scheduling, which is typical of the industry. In this work, an efficient algorithm for calculating critical plane factors, useful to speed up the fatigue assessment process, is presented. The algorithm applies to all critical plane factors that require the maximization of a specific parameter based on stress and strain components or a combination of them. The methodology maximizes the parameter utilizing tensor invariants and coordinates transformation law. In order to validate the proposed methodology, without loosing generality, the *Fatemi-Socie* critical plane factor was considered. The new algorithm was tested on different geometries (i.e. hourglass, notched and welded joint geometries) under different loading conditions (i.e. proportional/non-proportional, uniaxial and multiaxial loading) and showed a significant reduction in computation time respect the standard plane scanning method, without any loss of solution accuracy.

1. Introduction

Material fatigue is a highly debated topic in the scientific and industrial community [1–5]. Fatigue failure accounts for the majority of in-service failures of components [6] and still represents a major design challenge. Fatigue loading in real applications is characterized by complexities such as variable amplitude, randomness and multiaxiality [7]. All these factors, together with stress/strain gradients have to be accounted for during the fatigue assessment of a part. In this context, the use of finite element analyses (FEA) is a useful tool able to consider the above-mentioned complex features [8–13]. Often the problem is approached by modelling the critical region (i.e. considering stress/strain gradients and multiaxiality) and by applying the correct load history (i.e. considering variable amplitude or randomness). However, depending on the model and load conditions, simulations can be time-consuming, both during the solution and post-processing phases, particularly when the damage is calculated and several approaches can be implemented. The damage can be evaluated in several ways, and the different methods are commonly grouped in energy-based [14–17] and local or global stress/strain-based [18–26]. Strain-based methods are more suitable for fatigue life assessments involving a low-cycle-fatigue regime, while stress-based methods are more often employed in the high-cycle-fatigue regime. Similarly, the energetic criteria are subdivided into strain–energy-based criteria for low-cycle-fatigue applications, stress–energy-based criteria for high-cycle-fatigue applications, while a combination of stress- and strain–energy is commonly employed for low- and high-cycle fatigue applications [27]. Especially in the context of local damage models, critical plane (CP) factors gained a lot of attention in the last decades [28–35]. The CP methodology requires the calculation of a damage factor while evaluating the plane that experiences the most extreme damage. This plane is called the critical plane and represents the material orientation over which the crack initially propagates. In this context, CP damage models are normally use to evaluate the fatigue damage until the crack initiation phase [36–39]. However, failure propagation analyses can be performed as well based on CP [40–42].

* Corresponding author at: Department of Civil and Industrial Engineering, University of Pisa, Pisa, Italy.
E-mail addresses: andrea.chiocca@unipi.it (A. Chiocca), francesco.frendo@unipi.it (F. Frendo), giuseppe.marulo@it.rheinmetall.com (G. Marulo).

https://doi.org/10.1016/j.ijmecsci.2022.107974
Received 24 August 2022; Received in revised form 23 November 2022; Accepted 23 November 2022
Available online 1 December 2022

Especially for three-dimensional models with complex load history and geometry, stress/strain tensors can be obtained directly through the use of FE programs, with regard to every load step and every node of the model. The standard CP search method requires, for a specific node, to scan several planes in the three-dimensional space. Each plane is identified by using two or more angles and this process is commonly carried out through the use of nested *for/end* loops, that although simple, require considerable computational time. The significant computational cost is mainly related to the definition of an angular increment during the iteration process, which has to be an optimum between the accuracy of results and an acceptable solution time. The iterative process is further slowed down as quantities unnecessary for the definition of the damage parameter are sometimes evaluated on each rotated plane.

Albeit the CP factor methodology provides information on both the level of damage and the critical location and direction of crack propagation, its implementation is therefore usually time-consuming. This process may have to be applied to as many nodes as the model contains. Although, in practice, only those nodes belonging to the critical region of the component are provided to the algorithm. However, defining the critical region *a priori* is not always possible, especially in the case of models with very complicated geometry, load histories and constraints.

To the best of the authors' knowledge very few research works were already developed aimed at reducing the CP factors' computational time. Some methods are based on the analytical or quasi-analytical calculation of parameters belonging to the considered damage factor and the identification of the directions where this parameter or the damage factor is maximized. Marques et al. [43] have developed an algorithm applicable to spectral methods where CP factors or direction of maximum stress variance are more efficiently tracked. This method utilizes analytical formulas, calculating only those spectral parameters related to the selected damage factor as a function of the rotation angles and the spectral parameters in the initial condition. As it will be shown, the method presented in this work belongs to this group.

Other methods pursue computational speed by calculating the CP factor only in specific planes, avoiding the *brutal-force* procedure of discretizing the entire CP space utilizing a fixed angular increment [44–49]. These methods involve the discretization of a sphere of unit radius, representing the infinite set of material plane orientations. Wentingmann et al. [50] have developed an algorithm to increase the speed of CP detection based on the segmentation with quad elements of a coarse Weber half sphere. In this case, the obtained result depends on the performance parameters set by the user, which are meant to give an optimal compromise between accuracy and computational cost. Similarly, Sunde et al. [51] has developed an adaptive scheme for densifying a triangular mesh around the elements where the greatest damage has been noticed.

In other cases, the loading condition to which the specimen is subjected to results in a reduced stress state (e.g. plane stress, plane strain, etc.) that allows a purely analytical formulation of the damage factor [52–54]. However, although this condition can often be found on the surface of a component, it is always necessary to use a specific reference frame orientation to obtain a reduced tensor configuration.

In this work, a methodology is presented to directly evaluate a CP damage parameter based on stress and strain tensors invariants and tensor coordinate transformation laws. The presented method may be successfully applied to CP factors that require the maximization of a specific parameter or a combination of them (e.g. σ, τ, ε, γ, $\Delta\sigma$, $\Delta\tau$, $\Delta\varepsilon$, $\Delta\gamma$, $\Delta\sigma\Delta\tau$, $\Delta\varepsilon\Delta\gamma$, etc.). The method can be applied for both proportional and non-proportional loading as the methodology has been developed to account for a single load cycle (i.e. peak-to-valley or valley-to-peak). In the case of a complex load history, it is sufficient to iteratively apply the presented method to each successive peak-to-valley, valley-to-peak pair derived from a specific cycle counting formulation.

In the first part of the paper, the methodology is explained together with all the necessary theoretical background needed to understand the workflow. In the second part, some case studies are presented, including an hourglass specimen, a notched specimen and a welded component, concerning different loading conditions. For all the presented test cases a comparison has been obtained between the standard way of calculating CP factors (i.e. planes scanning) and the methodology presented in this work, both from a solution accuracy and computational-cost point of view. As it will be explained, the study conducted within this article refers to damage parameters that allows a closed-form solution of the CP factor calculation under all possible loading conditions (i.e. proportional and non-proportional).

Table 1
List of critical parameters on which the theory can be applied underlining the parameters to be maximized on that plane.

Damage model	Formula	Constants	Maximize
Fatemi-Socie [23]	$\frac{\Delta\gamma}{2}\left(1+k\frac{\sigma_{n,max}}{S_y}\right)$	k, σ_y	$\Delta\gamma$
Smith-Watson–Topper [26]	$\sigma_{n,max}\frac{\Delta\varepsilon}{2}$	–	$\Delta\varepsilon$
Kandil–Brown–Miller [25]	$\frac{\Delta\gamma}{2}+S\varepsilon_{n,max}$	S	$\Delta\gamma$
Chen–Xu–Huang I [58]	$\frac{\Delta\varepsilon}{2}\frac{\Delta\sigma_{n,max}}{2}+$ $+\frac{\Delta\tau_{n,max}}{2}\frac{\Delta\gamma_{n,max}}{2}$	–	$\Delta\varepsilon$
Chen–Xu–Huang II [58]	$\frac{\Delta\varepsilon_{n,max}}{2}\frac{\Delta\sigma_{n,max}}{2}+$ $+\frac{\Delta\tau_{n,max}}{2}\frac{\Delta\gamma}{2}$	–	$\Delta\gamma$
Liu I [59]	$(\Delta\sigma\Delta\varepsilon)_{max}+$ $+(\Delta\tau\Delta\gamma)$	–	$\Delta\sigma\Delta\varepsilon$
Liu II [59]	$(\Delta\sigma\Delta\varepsilon)+$ $+(\Delta\tau\Delta\gamma)_{max}$	–	$\Delta\tau\Delta\gamma$

2. General background on CP factors evaluation

In the following, for the sake of clarity and without loosing generality, the *Fatemi-Socie* CP factor (FS) [23] will be considered as a reference:

$$FS=\frac{\Delta\gamma}{2}\left(1+k\frac{\sigma_{n,max}}{S_y}\right) \tag{1}$$

where k is the material parameter found by fitting the uniaxial experimental data against the pure torsion data, $\Delta\gamma$ is the shear strain range, $\sigma_{n,max}$ is the normal stress acting on the plane where the shear strain range is evaluated and S_y is the material yield strength.

There are two possible applications based on the FS parameter as depicted in Fig. 1; the first one (case **A** in Fig. 1), consists in maximizing $\Delta\gamma$,[1] the second one involves maximizing the whole FS parameter [56] (case **B** in Fig. 1). This work deals with all the CP parameters that can be reconducted to case **A** and in this case a closed-form solution is always possible (i.e. for every load scenario), as it will be shown in the following. To this aim, Table 1 provides some other CP methods to which the presented methodology can be applied along with their formulas, the material-dependent parameters and the parameters to be maximized. Table 1 is not intended to be an exhaustive list, as the purpose of this work is to present the methodology and not the CP methods to which it can be applied to. For the parameters that can be reconducted to case **B** (such as the second formulation of FS or the Findley CP method [57]) a closed form solution is not possible and the way a numerical approximate solution can be obtained will be part of a future work.

Also the scheme of Fig. 1 is not intended to be exhaustive in describing all the possibilities for calculating CP factors, however it can represent a large majority of them.

[1] i.e. as the original formulation of FS method [23,55].

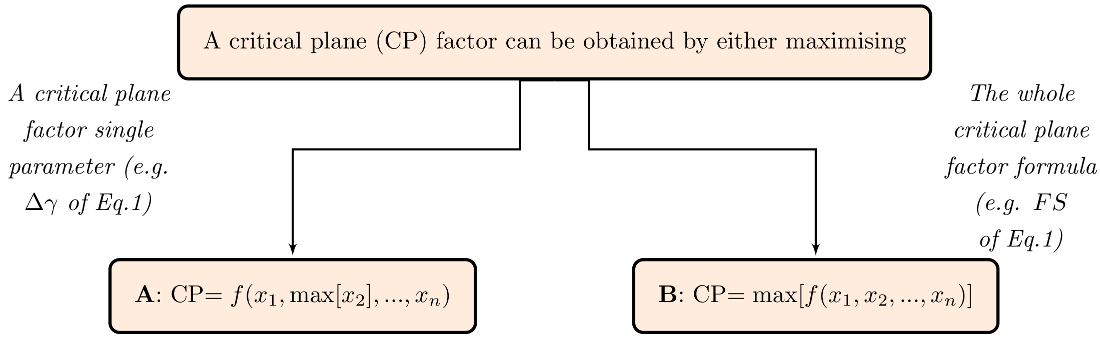

Fig. 1. Flowchart illustrating two key approaches for calculating a generic CP factor.

3. Standard plane scanning method for CP factor evaluation

In the following section, the standard method of plane scanning will be explained by presenting a typical procedure adopted in the literature for calculating the CP factor. Generally speaking, the fatigue strength of the material is dependent on the time evolution of the stress and strain tensors $\boldsymbol{\sigma}(t)$ and $\boldsymbol{\varepsilon}(t)$, given in Eq. (2). The stress and strain tensors can be evaluated for every possible point in the volume of the component, which can be approximated by nodes or integration points in finite element models.

$$\boldsymbol{\sigma}(t) = \begin{bmatrix} \sigma_{xx}(t) & \tau_{xy}(t) & \tau_{xz}(t) \\ \tau_{yx}(t) & \sigma_{yy}(t) & \tau_{yz}(t) \\ \tau_{zx}(t) & \tau_{zy}(t) & \sigma_{zz}(t) \end{bmatrix}, \ \boldsymbol{\varepsilon}(t) = \begin{bmatrix} \varepsilon_{xx}(t) & \frac{\gamma_{xy}}{2}(t) & \frac{\gamma_{xz}}{2}(t) \\ \frac{\gamma_{yx}}{2}(t) & \varepsilon_{yy}(t) & \frac{\gamma_{yz}}{2}(t) \\ \frac{\gamma_{zx}}{2}(t) & \frac{\gamma_{zy}}{2}(t) & \varepsilon_{zz}(t) \end{bmatrix} \tag{2}$$

The tensors of Eq. (2) refer to a general reference system $Oxyz$ and present a symmetry which bring to six the variable to be defined. The stress and strain tensors may describe a general multiaxial loading condition (i.e. fully populated) or simpler (i.e. not fully populated) state of stress and strain, such as uniaxial or biaxial (e.g. plane stress, plane strain) condition; Eq. (2) being the most general representation of a state of stress and strain in time-domain. However, respect to the time dependency of the tensor, the load-history can present different peculiarities. The stress components may be proportional or non-proportional, meaning that the principal stress directions are fixed in space, or vary with time, respectively. In addition, the load-time history can present periodicity, with constant or variable (in a deterministic or random way) amplitude. Using the tensors of Eq. (2), it is possible to derive all values of stress and strain for each direction in the space. Computationally this is accomplished in a discrete way by defining a plane Γ and its unit normal vector $\mathbf{n}$, thus being able to derive e.g., the stress normal to the plane σ_n and the shear strain γ on that plane, as shown in Fig. 2a–b for the specific case of the *Fatemi-Socie* CP factor. While iteratively rotating the Γ plane by a fixed angular step through the angles θ and ψ, it is possible to obtain a precise evaluation of stresses and strains in all directions. Fig. 2c shows the spatial distribution of the unit vector's tip $\mathbf{n}$ caused by the step-based rotation sequence.

4. Efficient method for the evaluation of CP factor and CP orientation

In the following section, the efficient method will be explained by presenting the underlying theoretical background. As commonly done during fatigue assessments, the load-time history will be considered as a discrete sequence of peaks and valleys instead of a continuous function over time t. In this framework, the stress and strain tensors $\boldsymbol{\sigma}^i$ and $\boldsymbol{\varepsilon}^i$ related to the generic ith loading condition (representing a peak or a valley) can be defined as

$$\boldsymbol{\sigma}^i = \begin{bmatrix} \sigma^i_{xx} & \tau^i_{xy} & \tau^i_{xz} \\ \tau^i_{yx} & \sigma^i_{yy} & \tau^i_{yz} \\ \tau^i_{zx} & \tau^i_{zy} & \sigma^i_{zz} \end{bmatrix}, \ \boldsymbol{\varepsilon}^i = \begin{bmatrix} \varepsilon^i_{xx} & \frac{\gamma^i_{xy}}{2} & \frac{\gamma^i_{xz}}{2} \\ \frac{\gamma^i_{yx}}{2} & \varepsilon^i_{yy} & \frac{\gamma^i_{yz}}{2} \\ \frac{\gamma^i_{zx}}{2} & \frac{\gamma^i_{zy}}{2} & \varepsilon^i_{zz} \end{bmatrix} \tag{3}$$

We can now identify two successive loading conditions as i and $i+1$, referring, for example, to a single sequence of peak and valley of the given load-history. At this point, it is possible to define the strain tensor range $\boldsymbol{\Delta\varepsilon}$ relative to the loading conditions i and $i+1$, as the difference between $\boldsymbol{\varepsilon}^i$ and $\boldsymbol{\varepsilon}^{i+1}$:

$$\boldsymbol{\Delta\varepsilon} = \boldsymbol{\varepsilon}^i - \boldsymbol{\varepsilon}^{i+1} \tag{4}$$

Both strain tensors $\boldsymbol{\varepsilon}^i$ and $\boldsymbol{\varepsilon}^{i+1}$ have to be defined with respect to the same reference system in order to calculate the strain tensor range; this is what usually done by an FE-program when stress and strain results are requested in a post-processing phase. By using the Mohr's representation (i.e., Fig. 3), the strain range tensor $\boldsymbol{\Delta\varepsilon}$ can be intended as the strain variation in every spatial direction for the given specific position into the model It is worth noting that the principal directions of all the three conditions of Fig. 3 are, in general, different, and, therefore, Fig. 3a cannot be obtained in graphical way, starting from Figs. 3b–3c.

Tensor properties can now be used to obtain the principal strain tensor range parameters ($\Delta\varepsilon_1$, $\Delta\varepsilon_2$ and $\Delta\varepsilon_3$), defined as the eigenvalues of the matrix $\boldsymbol{\Delta\varepsilon}$

$$\boldsymbol{\Delta\varepsilon} = \begin{bmatrix} \Delta\varepsilon_{xx} & \frac{\Delta\gamma_{xy}}{2} & \frac{\Delta\gamma_{xz}}{2} \\ \frac{\Delta\gamma_{yx}}{2} & \Delta\varepsilon_{yy} & \frac{\Delta\gamma_{yz}}{2} \\ \frac{\Delta\gamma_{zx}}{2} & \frac{\Delta\gamma_{zy}}{2} & \Delta\varepsilon_{zz} \end{bmatrix} = \begin{bmatrix} \Delta\varepsilon_1 & 0 & 0 \\ 0 & \Delta\varepsilon_2 & 0 \\ 0 & 0 & \Delta\varepsilon_3 \end{bmatrix} \tag{5}$$

As it can be observed from Fig. 3 the value of $\Delta\gamma_{max}$ (i.e. identifiable by an angle $2\omega = \frac{\pi}{2}$ on the Mohr's diagram) can be directly computed using the principal strain variations as follows

$$\frac{\Delta\gamma_{max}}{2} = \frac{(\Delta\varepsilon_1 - \Delta\varepsilon_3)}{2} \tag{6}$$

In order to compute the FS CP factor, it is necessary to evaluate the normal directions to $\Delta\gamma_{max}$ planes. To this regard, it is convenient to define the principal directions ($\mathbf{n_1}$, $\mathbf{n_2}$ and $\mathbf{n_3}$) related to the principal strain range parameters, which are defined as the eigenvectors of the matrix $\boldsymbol{\Delta\varepsilon}$

$$\mathbf{n_1} = \begin{bmatrix} n_{11} \\ n_{21} \\ n_{31} \end{bmatrix}; \ \mathbf{n_2} = \begin{bmatrix} n_{12} \\ n_{22} \\ n_{32} \end{bmatrix}; \ \mathbf{n_3} = \begin{bmatrix} n_{13} \\ n_{23} \\ n_{33} \end{bmatrix} \tag{7}$$

These directions define the principal coordinate system of the strain tensor range $\boldsymbol{\Delta\varepsilon}$. It is therefore straightforward to define the rotation matrix R_p defining the rotation from the global reference frame to the principal reference frame as

$$R_p = \begin{bmatrix} n_{11} & n_{12} & n_{31} \\ n_{21} & n_{22} & n_{32} \\ n_{31} & n_{23} & n_{33} \end{bmatrix} \tag{8}$$

```
for 0 < θ < π
    for 0 < ψ < π
        R = Rot_x(θ)Rot_y(ψ)
        n = R(:, 3)
        for 0 < α < π
            q = [cos(α); sin(α); 0]
            q = Rq
            σ_n(t) = n^T σ(t)n
            σ_n(t + dt) = n^T σ(t + dt)n
            γ(t) = q^T ε(t)n
            γ(t + dt) = q^T ε(t + dt)n
            FS = 0.5|γ(t) − γ(t + dt)| (1 + k max(σ_n(t), σ_n(t+dt)) / σ_y)
```

(a)

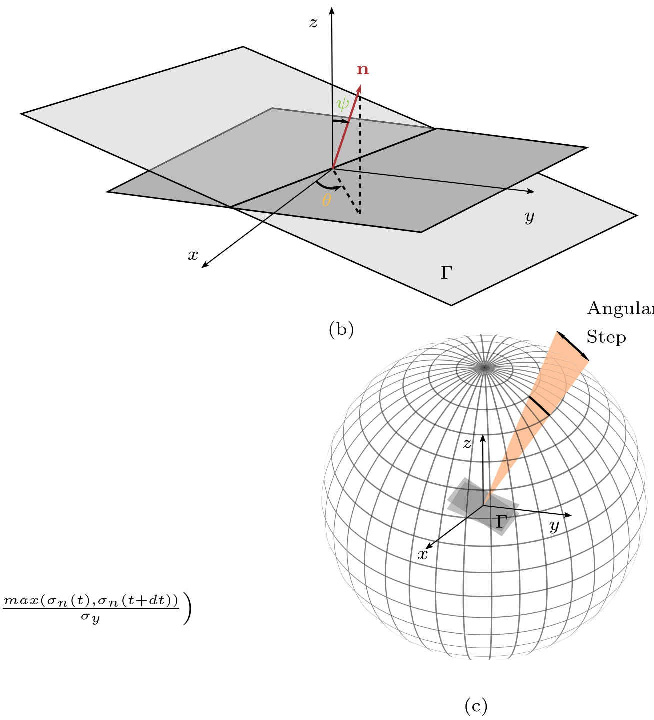

Fig. 2. Sample code for the evaluation of CP factor and CP orientation for the standard plane scanning method (a), plane configuration along with the most important parameters (b) and illustration of spatial distribution of the versor **n** normal to the plane Γ.

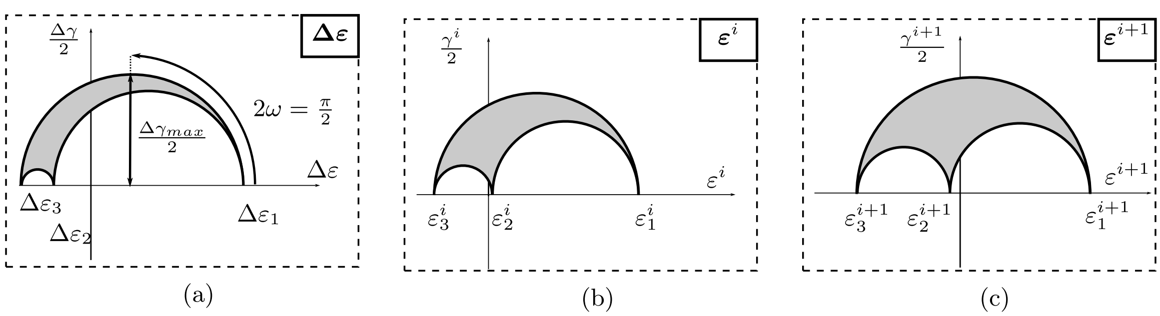

Fig. 3. Graphical exemplification of tensors using Mohr representation: strain tensor range $\boldsymbol{\Delta\varepsilon}$ (a), strain tensor relative to the ith loading condition $\boldsymbol{\varepsilon}^i$ (b) and strain tensor relative to the $(i+1)th$ loading condition $\boldsymbol{\varepsilon}^{i+1}$ (c).

With reference to Fig. 3, it is now possible to obtain the plane with maximum shear strain range by rotating of an angle $\omega = \frac{\pi}{4}$ about $\mathbf{n_2}$ (i.e., illustrated also in next Fig. 4). This rotation correspond to a $\frac{\pi}{2}$ rotation in the Mohr's diagram, with reference to the maximum diameter circumference. More formally, it represents an intrinsic rotation about the local y-axis and can be easily described by a rotation about $\mathbf{n_2}$-axis of the principal reference frame:

$$R_y = \begin{bmatrix} \cos(\frac{\pi}{4}) & 0 & \sin(\frac{\pi}{4}) \\ 0 & 1 & 0 \\ -\sin(\frac{\pi}{4}) & 0 & \cos(\frac{\pi}{4}) \end{bmatrix} \tag{9}$$

Then, the final rotation matrix R describing the new reference frame identifying $\Delta\gamma_{max}$ plane is obtainable by a rotation matrices concatenation:

$$R = R_p R_y = \begin{bmatrix} n_{11}\cos(\frac{\pi}{4}) - n_{13}\sin(\frac{\pi}{4}) & n_{12} & n_{11}\sin(\frac{\pi}{4}) + n_{31}\cos(\frac{\pi}{4}) \\ n_{21}\cos(\frac{\pi}{4}) - n_{32}\sin(\frac{\pi}{4}) & n_{22} & n_{21}\sin(\frac{\pi}{4}) + n_{32}\cos(\frac{\pi}{4}) \\ n_{31}\cos(\frac{\pi}{4}) - n_{33}\sin(\frac{\pi}{4}) & n_{23} & n_{31}\sin(\frac{\pi}{4}) + n_{33}\cos(\frac{\pi}{4}) \end{bmatrix} = \begin{bmatrix} r_{11} & r_{12} & r_{13} \\ r_{21} & r_{22} & r_{23} \\ r_{31} & r_{32} & r_{33} \end{bmatrix} \tag{10}$$

The above described procedure allows to compute $\Delta\gamma_{max}$ and the CP orientation directly by a single step. The reference frame $O'x'y'z'$ defining $\Delta\gamma_{max}$ plane is defined as

$$\mathbf{x}' = \begin{bmatrix} r_{11} \\ r_{21} \\ r_{31} \end{bmatrix}; \ \mathbf{y}' = \begin{bmatrix} r_{12} \\ r_{22} \\ r_{32} \end{bmatrix}; \ \mathbf{z}' = \begin{bmatrix} r_{13} \\ r_{23} \\ r_{33} \end{bmatrix} \tag{11}$$

Due to the symmetry of the strain tensor range, the maximum stress normal to the $\Delta\gamma_{max}$ planes may occur along the $x'-$ or z'-axis (see Fig. 4) and can then be computed as follows, considering both the ith and the $i+1$th load conditions.:

$$\sigma_{n,max} = \max\left(\max(\mathbf{x}'^T\boldsymbol{\sigma}^i\mathbf{x}',\ \mathbf{z}'^T\boldsymbol{\sigma}^i\mathbf{z}'), \max(\mathbf{x}'^T\boldsymbol{\sigma}^{i+1}\mathbf{x}',\ \mathbf{z}'^T\boldsymbol{\sigma}^{i+1}\mathbf{z}')\right) \tag{12}$$

The above described method, which involves matrix operations in relation to the strain tensor, cannot be applied to criteria, such as that represented by the Findley parameter, which are defined by a combination of the stress (or strain) tensor and a parameter, i.e. the normal stress, acting on the critical plane (these CP parameters belong to case **B** in Fig. 1). For those cases the Mohr's representation cannot be pursued and a numerical approach has to be developed.

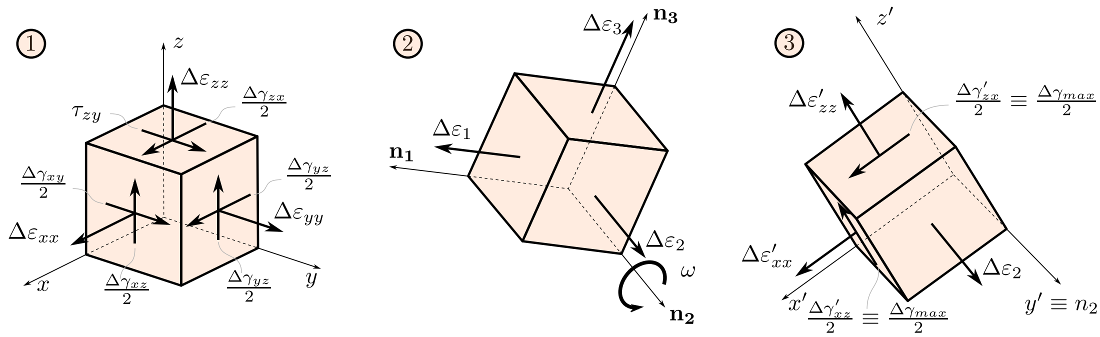

Fig. 4. Strain tensor rotations represented through the infinitesimal cubic material element; general reference system resulting from the export of results from the FE-analysis (1), principal reference system (2) and rotated reference system to obtain the $\Delta\gamma_{max}$ (3).

5. Methods benchmarking

With the purpose of comparing $\Delta\gamma_{max}$ and CP direction between the above described method and the standard spatial span iteration of angles, it is necessary to obtain a consistent angle triplet between the two above mentioned methodologies.

In this work the spatial span was described by intrinsic rotations about the axes xyz described by the Tait–Bryan angles θ, ψ, α respectively, through the rotation matrix $R_{xyz}(\theta,\psi,\alpha)$ [60]. The first two rotations about x-axis and y-axis identified the plane and the third rotation about z-axis identified the $\Delta\gamma$ direction on that plane. It is worth noting that the chosen rotation sequence xyz represent just one of the possible rotation sequences that can be used. In order to obtain the angles given by the coordinate transformation from the absolute to the rotated frame it is necessary to match the rotation matrices $R = R_{xyz}$. At this point it is possible to derive the relationships between angles and the matrix R coefficients as presented in Eq. (13)

$$r_{11} = \cos(\psi)\cos(\alpha),\ r_{12} = \cos(\psi)\sin(\alpha),\ r_{13} = \sin(\psi),$$
$$r_{23} = \sin(\theta)\cos(\psi),\ r_{33} = \cos(\theta)\cos(\psi),\ r_{11}^2 + r_{12}^2 = \cos(\psi) \quad (13)$$

Starting from Eq. (13) it is straightforward to derive the angles θ, ψ, α, as shown in Eqs. (14)–(16)

$$\theta = \arctan2(-r_{23}, r_{33}) \quad (14)$$

$$\psi = \arctan2(r_{13}, \sqrt{r_{11}^2 + r_{12}^2}) \quad (15)$$

$$\alpha = \arctan2(-r_{12}, r_{11}) \quad (16)$$

The angles presented in Eqs. (14)–(16) will later be used in Section 7 for direct comparison with the standard method.

It should be clear from the previous discussion, that the efficient method is based on the evaluation of a tensor range, starting from two different loading conditions, representing a fatigue cycle in the stress time-history. Once the time-history is known, even in the presence of material plasticity, load non-proportionality or residual stresses, the method can be directly applied. In practice, the method requires the identification of the two load configurations defining a fatigue cycle; to make the method viable for generic load histories, it must be iteratively applied to successive cycles. All the assumptions of material plasticity, load non-proportionality and residual stresses will simply affect the values of the stress and strain tensors at those identified load configuration steps.

6. Material and test cases

In this section three case studies will be presented and discussed. The model geometries and loading conditions were chosen in such a way to analyse most of the existing structural problems, thus providing reliable and exhaustive results. An hourglass specimen, a notched specimen and a (pipe-to-plate) welded joint were considered. The hourglass and notched specimens were loaded under tensile, torsion and combined tensile–torsion loading, while the welded joint under bending, torsion and combined bending–torsion loading. In all the three cases elastic–plastic material properties were implemented in the finite element simulations, thus to verify the applicability of the method even under material-plasticity. Fig. 5a shows the technical drawing of the hourglass specimen whose geometry was based on the ASTM E466 with a minimum diameter of 12 mm. Fig. 5b reports the notched specimen geometry, described by a notch radius of 0.2 mm and a minimum diameter of 16 mm. Fig. 5c shows the welded joint geometry composed by a tube, a reinforcement circular plate and a quadrangular base plate. The weld bead of interest for our work was the one between the tube and the base plate. Both the notched specimen and the welded joint components have already been part of a research project carried out by the same authors, where the fatigue endurance of such components have been studied under different loading conditions and in presence of residual stresses [10–12,61–64].

Table 2
Elastic-perfectly-plastic material properties implemented in the hourglass and notched specimen FE-models.

Young's modulus, E (MPa)	Poisson's ratio, ν (–)	Yield strength, σ_y (MPa)	Tangent modulus, E_T (MPa)
210 000	0.3	360	2000

Table 3
Elastic–plastic material properties implemented in the welded joint FE-model.

Young's modulus, E (MPa)		Poisson's ratio, ν (–)	
210 000		0.3	
Total strain, ε (–)	Stress, σ (MPa)	Total strain, ε (–)	Stress, σ (MPa)
0	0	0.00243	325
0.0004761	100	0.00295	350
0.000629	125	0.00361	375
0.000762	150	0.00445	400
0.000904	175	0.00551	425
0.001060	200	0.00685	450
0.001237	225	0.00851	475
0.001448	250	0.01058	500
0.001705	275	0.01311	525
0.00202	300	0.01994	575

6.1. Finite element analysis

All the above mentioned components were studied by means of FE-analyses using the second release of the software Ansys©2021. Static structural analysis were performed, under the assumption of small displacements. The material considered for all three case studies was a structural steel S355. Material non-linearity was introduced in the analysis by assuming a bilinear elastic–plastic material behaviour for

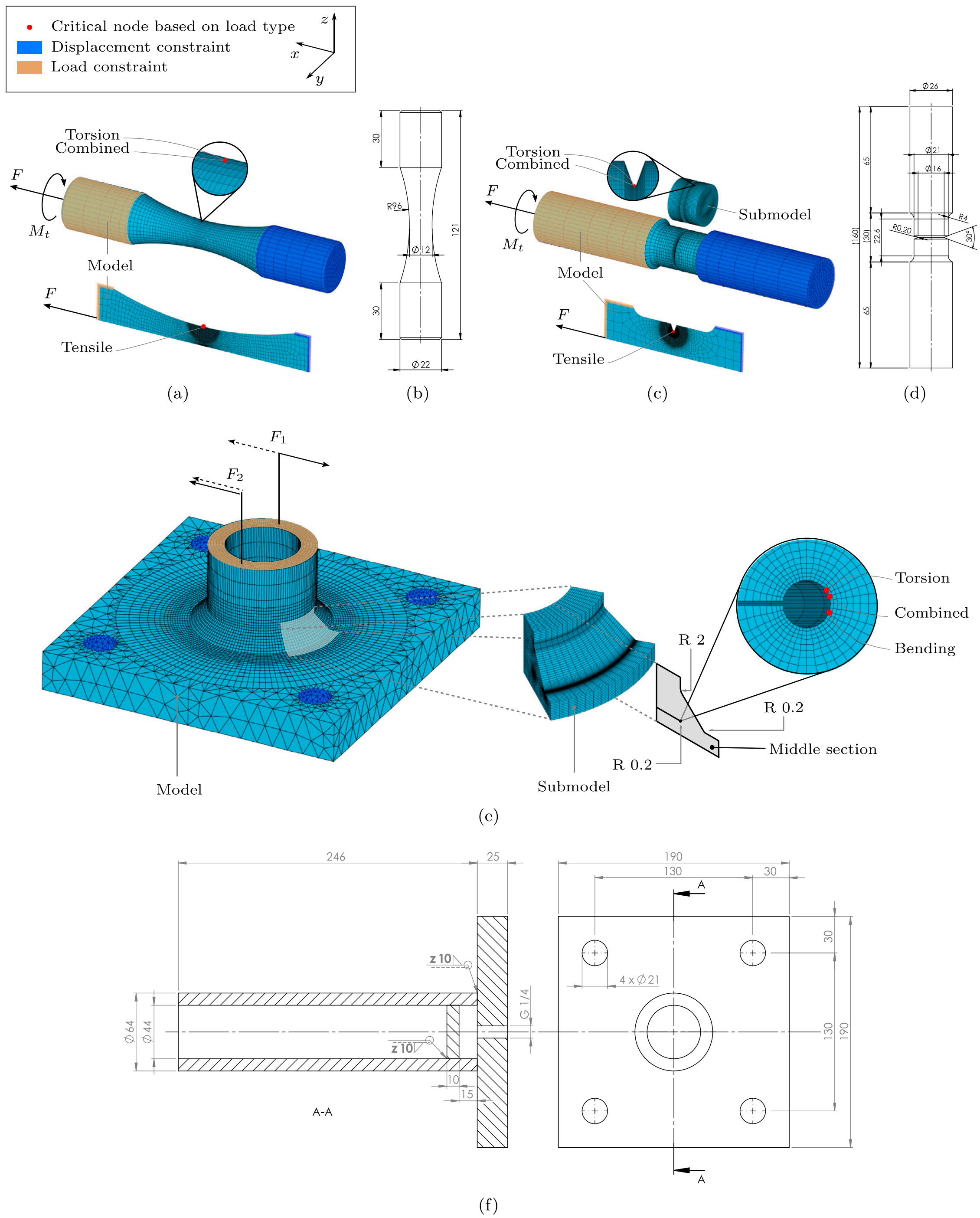

Fig. 5. Finite element model (a) and technical drawing (b) of the hourglass specimen; finite element model (c) and technical drawing (d) of the notched specimen; finite element model (e) and technical drawing (f) of the welded joint; the FE-models present the position on which the $\Delta\gamma$ resulted the maximum under the different loading conditions.

the hourglass and notched specimen, as reported in Table 2 and a multi-linear elastic–plastic material behaviour in the case of the welded joint, as shown in Table 3. The material properties were obtained from Tsavdaridis et al. [65] and Lopez and Fatemi [66] in the case of bilinear and multi-linear cyclic material behaviour, respectively .

The FE-models were all three-dimensional and employed 3D structural brick elements (i.e. SOLID186 in Ansys) with 20 nodes and quadratic shape functions, with the exception of the hourglass and notched specimens loaded in traction/compression, in which the loads and constraints allowed the use of an axisymmetry assumption; in this case, 2D structural plane elements (i.e. PLANE183 in Ansys) with 8 nodes and quadratic shape function were employed. Every node has three degrees of freedom (i.e. the displacements in the three spatial directions x, y and z) if three-dimensional elements were employed, while two degrees of freedom (i.e. the displacements in the two spatial directions defining the working plane x and y) for the two-dimensional elements.

The hourglass specimen mesh was modelled with 336 134 nodes and 81 018 elements for the three-dimensional geometry and 24 276 nodes and 7991 elements for the two-dimensional geometry. The three-dimensional notched specimen model employed a submodeling analysis in order to better optimize the mesh in the notch region. A number of 123 170 nodes and 29 234 elements for the three-dimensional model and 351 974 nodes and 84,900 elements for the submodel were used,

Table 4
Load steps combination used during simulations with F referring to the applied force and M_t referring to the torque shown in Fig. 5.

Load type	Hourglass specimen		Notched specimen		Welded joint	
	Load step n.1	Load step n.2	Load step n.1	Load step n.2	Load step n.1	Load step n.2
Case 1	F =19 kN M_t =0 N m	F =76 kN M_t =0 N m	F =5.3 kN M_t =0 N m	F =53 kN M_t =0 N m	F_1 =−5.7 kN F_2 =−5.7 kN	F_1 =5.7 kN F_2 =5.7 kN
Case 2	F =0 kN M_t =10 N m	F =0 kN M_t =100 N m	F =0 kN M_t =10 N m	F =0 kN M_t =80 N m	F_1 =−15 kN F_2 =15 kN	F_1 =15 kN F_2 =−15 kN
Case 3	F =140 kN M_t =0 N m	F =0 kN M_t =100 N m	F =31.8 kN M_t =0 N m	F =0 kN M_t =80 N m	F_1 =3.4 kN F_2 =3.4 kN	F_1 =11 kN F_2 =−11 kN

Table 5
Graphical overview of the main normal and shear stress components pattern over load steps.

Load type	Hourglass specimen	Notched specimen	Welded joint
Case 1	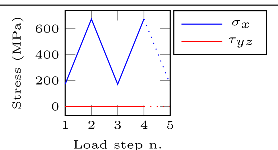	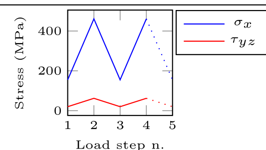	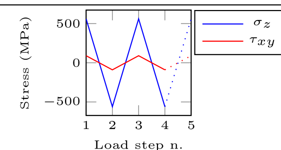
Case 2	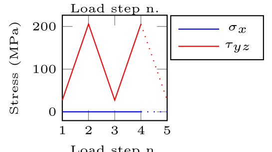	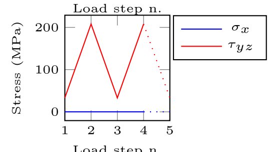	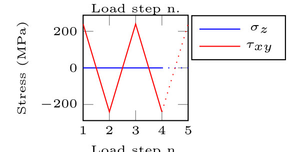
Case 3	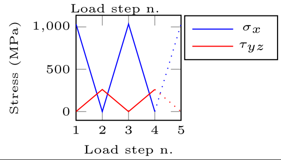	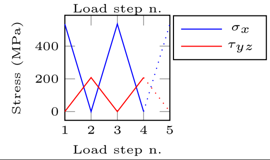	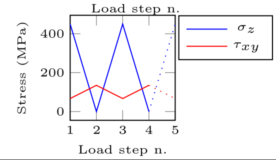

respectively. With regard to the two-dimensional notched specimen model 38 897 nodes and 12 888 elements were used in the FEA. A submodel analysis was used for the welded joint too, thus to better describe the stress and strain state in the weld notches (i.e. weld toes and weld root). The submodel details a model slice of 54° opening angle, and includes part of the base plate, part of the pipe, and the whole section of the weld bead. In this case 96 420 nodes and 97 728 elements and 155 454 nodes and 35 408 elements were used in the model and submodel, respectively. The mesh size reported above for all FE-models was achieved after a convergence analysis. As a convergence criterion, a difference lower than 5% was attained on the maximum von Mises stress in the critical regions of the FE-models (i.e. the area where the stress and strain values were obtained for the successive analysis).

The different loading conditions, both proportional and non proportional, where obtained by applying forces, moments or a combination of them together with fixed supports on the appropriate surfaces, as exemplified in Fig. 5. For the hourglass and notched specimen the cylindrical surfaces were used for applying the boundary conditions, while the top tube surface and the plate holes were used in the case of the welded joint. The load sequences reported in Table 4 were applied and include two proportional loading (i.e. axial/bending and torsion, respectively) conditions and a non proportional loading condition, with a 90° phase angle between bending and torsion load. Each column of the table reports the combination of forces/moment applied to a specific specimen geometry (i.e. hourglass specimen, notched specimen and welded joint) in a particular loading condition (i.e. tensile/bending, torsion and combined tensile/bending–torsion loading). In the following the loading conditions will be designated as:

- Proportional loading *case 1*, tensile loading for hourglass and notched specimen geometries and bending loading for the welded joint;
- Proportional loading *case 2*, torsional loading for all specimen geometries;
- Non proportional loading *case 3*, combined out-of-phase tensile and torsion loading for hourglass and notched specimen geometries and combined out-of-phase bending and torsion loading for the welded joint geometry.

The load conditions that were considered are intended to exemplify the majority of in-service loads that can be encountered by the analyst. The maximum normal and tangential stress components resulting from the loads in Table 4 are presented in Table 5 consistently for each combination of geometry and load with regard to the reference frame presented in Fig. 5. Especially in the case of fatigue investigations under non-proportional loading conditions it may become challenging the identification of two subsequent steps in the load-history needed to compute the parameter range. However, non-proportional cycle counting methods can be applied such as the well-known Wang–Brown [67, 68] based on a modified equivalent strain theory, or the recent one proposed by Janssens [69]. On the other side, it is worth noting that the well known Bannantine and Socie's [70] multiaxial cycle counting method cannot be applied. In fact, the Bannantine and Socie's method apply the standard cycle counting (e.g. rainflow) to the projected normal or shear strain on the failure plane that, therefore, requires to be identified based on an iterative process of damage calculation through all possible plane orientations, by the usual scanning process.

For the analysed cases of Table 4, loads were defined in such a way that all the components critical locations behave elastically during the first load step, while material plasticity occurs during the second load step if tensile/bending or torsion loading were applied, separately. On the contrary, the material undergoes plasticity in the critical nodal locations, during both load steps, when the components were loaded under combined tensile–torsion for notched and hourglass specimens or under combined bending–torsion for the welded joint.

6.2. Scripts implementation

The calculation of the *Fatemi-Socie* CP factor was carried out by implementing the formulas in a Matlab® script, both for the standard for $i = LoadStep$ and $j = LoadStep + 1$

$$\Delta E = E(i) - E(j)$$

$$\Delta\varepsilon_1, \Delta\varepsilon_2, \Delta\varepsilon_3 = eigenvalue(\Delta E)$$

$$R = eigenvector(\Delta E)$$

$$R = R\,Rot_y(\omega) \text{ with } \omega = \frac{\pi}{4}$$

$$\mathbf{n_1} = R(:,1)$$

$$\mathbf{n_3} = R(:,3)$$

$$\Delta\gamma_{max} = \Delta\varepsilon_1 - \Delta\varepsilon_3$$

$$\sigma_{n,max} = max(\mathbf{n_1}^T S(i)\mathbf{n_1}, \mathbf{n_1}^T S(j)\mathbf{n_1}, \mathbf{n_3}^T S(i)\mathbf{n_3}, \mathbf{n_3}^T S(j)\mathbf{n_3})$$

$$FS = 0.5\Delta\gamma_{max}\left(1 + k\frac{\sigma_{n,max}}{\sigma_y}\right)$$

(a)

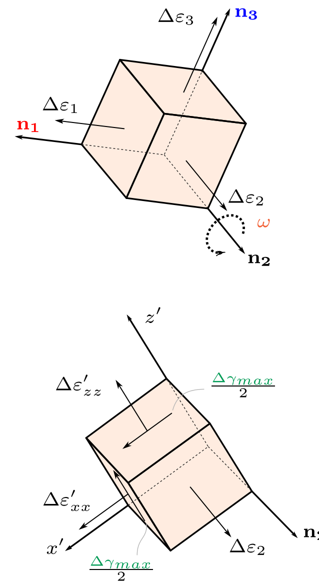

(b)

Fig. 6. Sample code for the evaluation of CP factor and CP directions for the efficient method (a) and main code parameters represented through the infinitesimal cubic material element (b).

iterative procedure and the proposed method, based on the shear strain tensor range. As already stated, the standard method involves nested *for/end* loops, which results in a massive slowdown of the calculation. The computational speed is mainly dependent on the angular step used during the loops. For our case, an angular step of 1° was used to perform the spatial scan of half sphere described by the angular ranges $0 < \theta < \pi$ and $0 < \psi < \pi$. The angular step of 1° provides an optimum between computational cost and accuracy as it yields to CP factor value convergence with an error lower than 1% [48,49].

The material-dependent parameters k and σ_y were assumed with values of 0.4 and 360 MPa respectively. The k was considered constant although recent works has identified a dependency on the number of cycles to failure of the material N_f [71–73]. However, as the primary purpose of our work was the comparison between the two methods, the introduction of a variable k would not have altered the comparative result but only increased the complexity of algorithm implementation. The codes which implement the CP calculation methods have common parts, such as the data import from the finite element analysis and the write-out of the final results. The calculation times presented in the next section do not include the plot generation, but only the necessary operations to obtain the $\Delta\gamma$ and the corresponding FS value. A concise script-flowchart presenting the efficient methodology is provided in the Fig. 6 as a support to the theoretical discussion given in Section 4. It is worth noting that the occurrence of an initial state of stress (i.e. residual stresses) would not invalidate the method presented above since only the stress and strain tensors during the two considered load steps are required for the CP evaluation. An initial state of stress would only change the values inside the considered tensors leaving unchanged the methodology to be applied.

7. Results and discussion

The following section provides an overview and discussion of the results concerning the CP factors calculated by means of the standard and the efficient method. The formulas introduced in Section 4 compute the required value explicitly, thus giving a mathematically correct solution and not a numerical approximation. This is visible in the results of Table 6, where $\Delta\gamma_{max}$ values calculated with the two methods have been compared. The percentage relative difference ($Rel.Diff\%$) obtained comparing the results has always been found to be smaller than 0.3%, which brings the error to be mainly numerical. The difference, although small, may be due to the numerical approximation of the standard method, which requires a finite angular step to determine the maximum damage value.

Similarly, Table 7, shows the comparison results of the FS values, obtained for the same CP of Table 7 determined by maximizing $\Delta\gamma$. In this case, slightly larger differences were found (contained below 1.3%), which can be attributed to approximations in σ_n values obtained by the scanning plane procedure. In this case a reduction in the angular range was found to lead to a large improvement in the results but with a large increase in the time required for the solution. For this reason the angular step was kept constant at a value of 1° thus admitting an error of about 1%.

The improvement in computation time is shown in Table 8. All the scripts were run in Matlab® environment on a 11th Gen Intel(R) Core(TM) i7 with 15 GB of RAM available and 4 cores. The PI parameter of Eq. (17) was used to indicate a performance index. The parameter PI is 100% when the efficient method time is zero or the standard method time is infinite and is 0% when there is no reduction in the computation time. This parameter represents the performance improvement in terms of time to evaluate the script. As it can be observed, a major time reduction was achieved with PI parameter always greater than 94.5% since the majority of *for/end* loops were omitted in the proposed efficient method; the stress and strain data for each load cycle have to be obtained only once.

$$PI = \left(1 - \frac{t_{efficient}}{t_{standard}}\right) \tag{17}$$

The computation time was reduced by an order of magnitude (i.e., from ≈ 7 s to ≈ 0.3 s) while implementing a non-optimized code on Matlab®; moving toward lower-level programming languages and by improving the code a further reduction of the computational time can be reasonably expected.

The comparison between the two methods in terms of CP orientation is shown in Fig. 7 with respect the hourglass specimen, Fig. 8 with respect to the notched specimen and Fig. 9 with respect to the welded

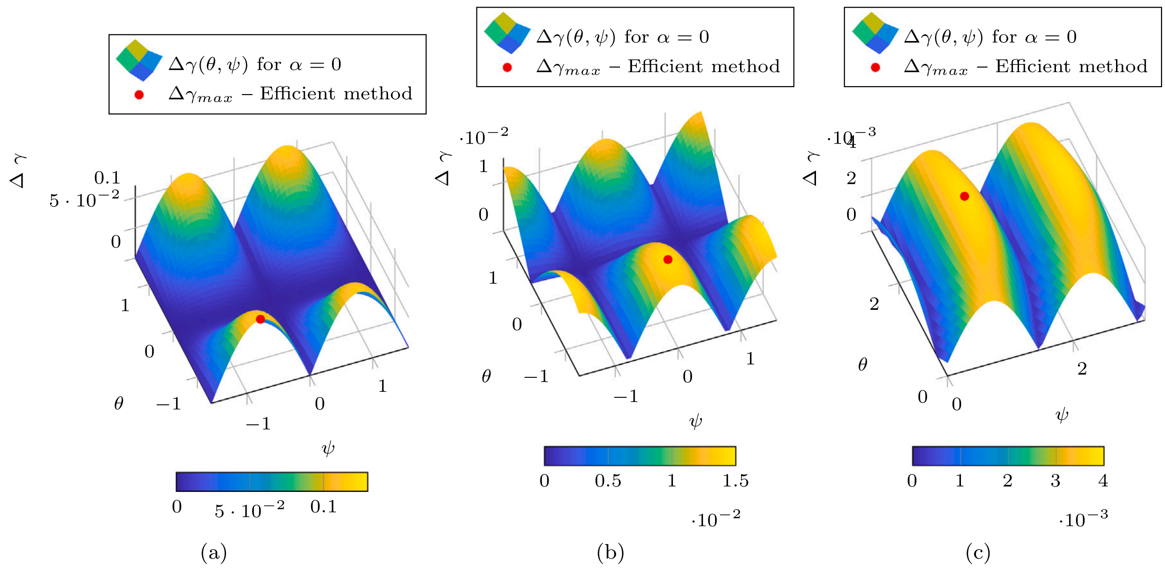

Fig. 7. Periodic solution of $\Delta\gamma$ resulting from the spatial span of angles θ, ψ and for a fixed value of α for tensile loading (a), torsional loading (b) and tensile–torsional loading (c) of the hourglass specimen geometry. The location of the $\Delta\gamma_{max}$ is shown in red: $\theta = -1.5708$, $\psi = -0.7854$, $\alpha = 0$ (a), $\theta = -1.1521$, $\psi = 0$, $\alpha = 0$ (b), $\theta = 1.9895$, $\psi = 1.0384$, $\alpha = 0$ (c).

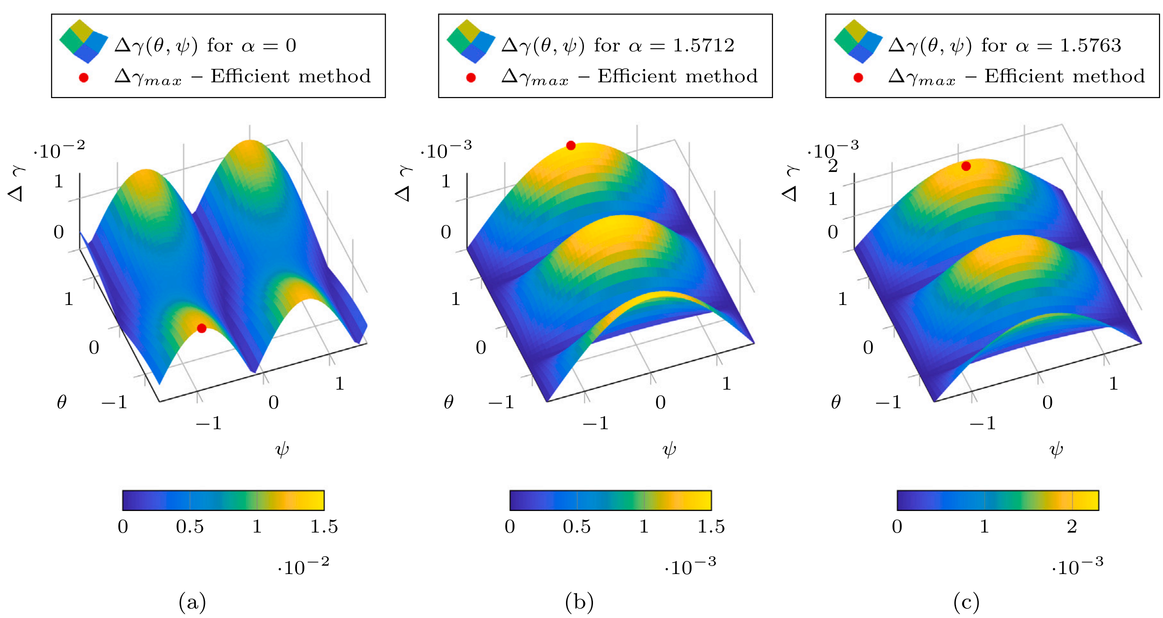

Fig. 8. Periodic solution of $\Delta\gamma$ resulting from the spatial span of angles θ, ψ and for a fixed value of α for tensile loading (a), torsional loading (b) and tensile–torsional loading (c) of the notched specimen geometry. The location of the $\Delta\gamma_{max}$ is shown in red: $\theta = -1.5708$, $\psi = -0.9311$, $\alpha = 0$ (a), $\theta = 1.5708$, $\psi = 0$, $\alpha = 1.5706$ (b), $\theta = 1.2674$, $\psi = 0.0033$, $\alpha = 1.5763$ (c).

Table 6
Comparison of $\Delta\gamma_{max}$ values between the efficient method and the standard one.

$\Delta\gamma_{max}$ comparison									
Load type	Hourglass specimen			Notched specimen			Welded joint		
	Efficient	Standard	$Rel.Diff.\%$	Efficient	Standard	$Rel.Diff.\%$	Efficient	Standard	$Rel.Diff.\%$
Case 1	0.1157	0.1158	0.086%	0.01213	0.01213	0%	0.00463	0.00463	0%
Case 2	0.01426	0.01427	0.021%	0.001465	0.001465	0%	0.00434	0.00434	0%
Case 3	0.00383	0.00382	0.26%	0.00206	0.00206	0%	0.00360	0.00360	0%

joint. A graphical comparison allows a clearer comprehension of the subject in this case. Figs. 7a–9a depict the tensile loading case for the hourglass and notched specimens and the bending loading for the welded joint. Figs. 7b–9b, instead, present the torsional loading case and Figs. 7c–9c, the combined loading case. In all scenarios a very good agreement was found regarding the CP orientation identified by the new method, represented by a red dot in all the Figures. All the red dots find their positioning precisely on the maxima of the coloured plots representing the $\Delta\gamma$ values deriving from the spatial span. Evidently, the solution found by the proposed efficient method is unique although the

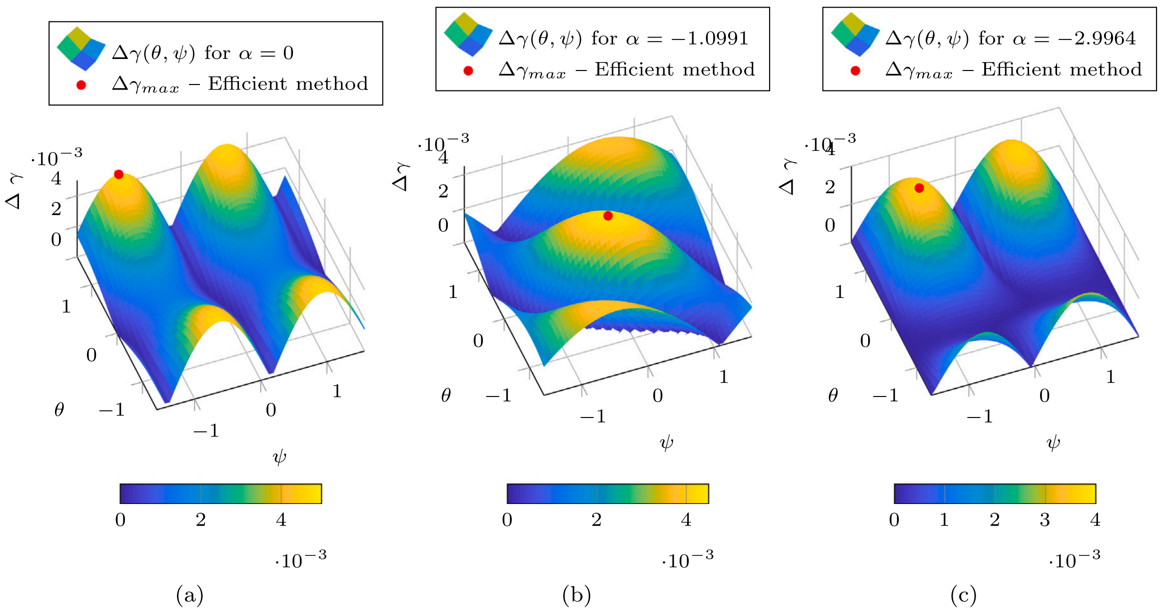

Fig. 9. Periodic solution of $\Delta\gamma$ resulting from the spatial span of angles θ, ψ and for a fixed value of α for bending loading (a), torsional loading (b) and bending–torsional loading (c) of the welded joint. The location of the $\Delta\gamma_{max}$ is shown in red: $\theta = 1.5708$, $\psi = -0.9419$, $\alpha = 0$ (a), $\theta = 0$, $\psi = 0$, $\alpha = -1.0991$ (b), $\theta = 0.9514$, $\psi = -0.7822$, $\alpha = -2.9964$ (c).

Table 7
Comparison of FS values between the efficient method and the standard one.

FS comparison									
Load type	Hourglass specimen			Notched specimen			Welded joint		
	Efficient	Standard	$Rel.Diff.\%$	Efficient	Standard	$Rel.Diff.\%$	Efficient	Standard	$Rel.Diff.\%$
Case 1	0.1608	0.1598	0.62%	0.01556	0.01547	0.58%	0.00627	0.00627	0%
Case 2	0.01426	0.01427	0.021%	0.001465	0.001465	0%	0.00434	0.00434	0%
Case 3	0.00716	0.00726	1.3%	0.00324	0.00324	0%	0.00481	0.00482	0.2%

Table 8
Comparison of computational cost between the efficient method and the standard one.

Computational time comparison									
Load type	Hourglass specimen			Notched specimen			Welded joint		
	Efficient	Standard	PI	Efficient	Standard	PI	Efficient	Standard	PI
Case 1	$t = 0.348$ s	$t = 7.270$ s	95.2%	$t = 0.364$ s	$t = 7.006$ s	94.8%	$t = 0.317$ s	$t = 7.249$ s	95.6%
Case 2	$t = 0.332$ s	$t = 7.247$ s	95.4%	$t = 0.315$ s	$t = 7.282$ s	95.6%	$t = 0.340$ s	$t = 7.264$ s	95.3%
Case 3	$t = 0.342$ s	$t = 7.151$ s	95.2%	$t = 0.396$ s	$t = 7.307$ s	94.5%	$t = 0.359$ s	$t = 7.284$ s	95.0%

surfaces often present periodic patterns in the studied angular range. Those pattern can clearly been recognized considering the loading case and the symmetry of the stress tensor; indeed the solution periodicity information can be recovered by simple consideration on the Cauchy's stress tensor.

As a final consideration on the method, it should be considered that the implementation of the described method can be further optimized from a computational-time point of view through a more fine-tuned programming which, however, is not part of this work. For this reason, the run-times shown in Table 8 may not be the optimal ones achievable. It is therefore up to the interested reader to implement the method on the most convenient coding programme. As a matter of fact, the model implementation is straightforward as it only makes use of basic tensor mathematics.

8. Conclusions

The presented work was intended to illustrate a comprehensive method to speed up the computation of CP factors; this can be of particular interest for industrial applications, or whenever a tight time schedule is imposed. The methodology is based upon the use of stress and strain tensor invariants and coordinates transformation law, and it was implemented in a ready to use Matlab® script. Different case studies have been presented in order to provide a significant variety of component geometry and loading conditions. The *Fatemi-Socie* critical plane factor has been used as a case study damage parameter. Based on the performed analyses and the results obtained, the following conclusions can be drawn:

- the method is rather general and can be applied to several critical plane factors in addition to the one presented (to all CP parameters that can be classified as case **A** in Table 1);
- the method can be implemented in case of uniaxial, multiaxial, proportional or non-proportional loading conditions and even in presence of residual stresses;
- the method allows a significant reduction in computation time, with respect to the standard scanning plane method, as it avoids the use of many nested *for/end* loops; a reduction in computation time always greater of 94.5% on a single node was obtained with reference to the examined test cases; such a reduction in computation time will potentially enable easier and more effective use of CP methods, even in industrial applications;

- compared with the standard plane scanning method, the proposed method provides a closed form solution for the critical plane and, consequently, for the damage parameter;
- the method is easy to operate and can be implemented in a variety of codes since it makes use of basic tensor math; the extension to other CP factors turns out to be fairly straightforward, as well.

For the evaluation of damage factors a reduced computation time, during the post-processing phase, is crucial as it allows a more complete and detailed evaluation of the studied model. In the present work, the method was applied only to those cases where an analytical solution is possible (i.e. case **A** of Fig. 1). However, in a similar fashion, it is also possible to tackle the problem of evaluating CP factors based on more complex formulation, for which a closed form solution cannot be obtained (i.e. case **B** of Fig. 1); this will be the subject of future works.

CRediT authorship contribution statement

A. Chiocca: Conceptualization, Methodology, Software, Formal analysis, Validation, Visualization, Investigation, Writing – original draft, Writing – review & editing. **F. Frendo:** Resources, Conceptualization, Methodology, Formal analysis, Writing – review & editing, Supervision, Data curation, Project administration. **G. Marulo:** Conceptualization, Formal analysis, Investigation, Methodology, Data curation.

Declaration of competing interest

The authors declare the following financial interests/personal relationships which may be considered as potential competing interests: Andrea Chiocca reports financial support was provided by Government of Italy Ministry of Education University and Research.

Data availability

Data will be made available on request.

Acknowledgements

This paper is supported by the Ministry of University and Research (MUR) as part of the PON 2014–2020 "Research and Innovation" resources – Green Action - DM MUR 1062/2021 - Title of the Research: Development and conversion of automotive devices towards sustainability: The decarbonisation of vehicles and new uses of thermo-hydraulic systems.

References

[1] Cowles BA. High cycle fatigue in aircraft gas turbines—an industry perspective. Int J Fract 1989;80(2):147–63. http://dx.doi.org/10.1007/BF00012667.

[2] Chu CC. Multiaxial fatigue life prediction method in the ground vehicle industry. Int J Fatigue 1997;19(SUPPL.1):325–30. http://dx.doi.org/10.1016/s0142-1123(97)00018-2.

[3] Kaldellis JK, Zafirakis DP. Trends, prospects, and R&D directions in wind turbine technology. In: Comprehensive renewable energy, vol. 2. Elsevier; 2012, p. 671–724. http://dx.doi.org/10.1016/B978-0-08-087872-0.00224-9.

[4] Koyama M, Zhang Z, Wang M, Ponge D, Raabe D, Tsuzaki K, et al. Bone-like crack resistance in hierarchical metastable nanolaminate steels. Science 2017;355(6329):1055–7. http://dx.doi.org/10.1126/science.aal2766.

[5] Xu L, Wang K, Yang X, Su Y, Yang J, Liao Y, et al. Model-driven fatigue crack characterization and growth prediction: A two-step, 3-D fatigue damage modeling framework for structural health monitoring. Int J Mech Sci 2021;195:106226. http://dx.doi.org/10.1016/j.ijmecsci.2020.106226.

[6] Bhaumik SK, Sujata M, Venkataswamy MA. Fatigue failure of aircraft components. Eng Fail Anal 2008;15(6):675–94. http://dx.doi.org/10.1016/j.engfailanal.2007.10.001.

[7] Kuncham E, Sen S, Kumar P, Pathak H. An online model-based fatigue life prediction approach using extended Kalman filter. Theor Appl Fract Mech 2022;117:103143. http://dx.doi.org/10.1016/j.tafmec.2021.103143.

[8] Palmieri M, Zucca G, Morettini G, Landi L, Cianetti F. Vibration fatigue of FDM 3D printed structures: The use of frequency domain approach. Materials 2022;15(3):854. http://dx.doi.org/10.3390/ma15030854.

[9] Chen F, Shang D-G, Li D-H, Wang L-W. Multiaxial thermo-mechanical fatigue life prediction based on notch local stress-strain estimation considering temperature change. Eng Fract Mech 2022;265:108384. http://dx.doi.org/10.1016/j.engfracmech.2022.108384.

[10] Frendo F, Marulo G, Chiocca A, Bertini L. Fatigue life assessment of welded joints under sequences of bending and torsion loading blocks of different lengths. Fatigue Fract Eng Mater Struct 2020;43(6):1290–304. http://dx.doi.org/10.1111/ffe.13223.

[11] Chiocca A, Frendo F, Bertini L. Evaluation of residual stresses in a tube-to-plate welded joint. In: MATEC web of conferences, vol. 300. EDP Sciences; 2019, p. 19005. http://dx.doi.org/10.1051/matecconf/201930019005.

[12] Chiocca A, Frendo F, Bertini L. Evaluation of residual stresses in a pipe-to-plate welded joint by means of uncoupled thermal-structural simulation and experimental tests. Int J Mech Sci 2021;199:106401. http://dx.doi.org/10.1016/j.ijmecsci.2021.106401.

[13] Meneghetti G, Campagnolo A, Visentin A, Avalle M, Benedetti M, Bighelli A, et al. Rapid evaluation of notch stress intensity factors using the peak stress method with 3D tetrahedral finite element models: Comparison of commercial codes. Fatigue Fract Eng Mater Struct 2022;45(4):1005–34. http://dx.doi.org/10.1111/ffe.13645.

[14] Lazzarin P, Berto F. Some expressions for the strain energy in a finite volume surrounding the root of blunt V-notches. Int J Fract 2005;135(1–4):161–85. http://dx.doi.org/10.1007/s10704-005-3943-6.

[15] Berto F, Lazzarin P. The volume-based strain energy density approach applied to static and fatigue strength assessments of notched and welded structures. In: Procedia engineering, vol. 1, no. 1. No longer published by Elsevier; 2009, p. 155–8. http://dx.doi.org/10.1016/j.proeng.2009.06.036.

[16] Mroziński S. Energy-based method of fatigue damage cumulation. Int J Fatigue 2019;121:73–83. http://dx.doi.org/10.1016/j.ijfatigue.2018.12.008.

[17] Varvani-Farahani A, Haftchenari H, Panbechi M. An energy-based fatigue damage parameter for off-axis unidirectional FRP composites. Compos Struct 2007;79(3):381–9. http://dx.doi.org/10.1016/j.compstruct.2006.02.013.

[18] European Committee for Standardization (CEN). Eurocode 3: Design of steel structures — Part 1-9: Fatigue, 50. 2005, p. 77.

[19] Hobbacher AF. The new IIW recommendations for fatigue assessment of welded joints and components - A comprehensive code recently updated. Int J Fatigue 2009;31(1):50–8. http://dx.doi.org/10.1016/j.ijfatigue.2008.04.002.

[20] Karakaş, Zhang G, Sonsino CM. Critical distance approach for the fatigue strength assessment of magnesium welded joints in contrast to Neuber's effective stress method. Int J Fatigue 2018;112:21–35. http://dx.doi.org/10.1016/j.ijfatigue.2018.03.004.

[21] Taylor D, Barrett N, Lucano G. Some new methods for predicting fatigue in welded joints. Int J Fatigue 2002;24(5):509–18. http://dx.doi.org/10.1016/S0142-1123(01)00174-8.

[22] Radaj D, Sonsino CM, Fricke W. Fatigue assessment of welded joints by local approaches. 2nd ed.. 2006, p. 1–639. http://dx.doi.org/10.1533/9781845691882.

[23] Fatemi A, Socie DF. A critical plane approach to multiaxial fatigue damage including out-of-phase loading. Fatigue Fract Eng Mater Struct 1988;11(3):149–65. http://dx.doi.org/10.1111/j.1460-2695.1988.tb01169.x.

[24] Findley WN. A theory for the effect of mean stress on fatigue of metals under combined torsion and axial load or bending. J Eng Ind 1959;81(4):301–5. http://dx.doi.org/10.1115/1.4008327.

[25] Kandil FA, Brown MW, J. MK. Biaxial low-cycle fatigue failure of 316 stainless steel at elevated temperatures. In: Mechanical behaviour and nuclear applications of stainless steel at elevated temperatures. London, UK: Maney Pub.; 1982.

[26] Socie D. Multiaxial fatigue damage models. J Eng Mater Technol Trans ASME 1987;109(4):293–8. http://dx.doi.org/10.1115/1.3225980.

[27] Macha E, Sonsino CM. Energy criteria of multiaxial fatigue failure. Fatigue Fract Eng Mater Struct 1999;22(12):1053–70. http://dx.doi.org/10.1046/j.1460-2695.1999.00220.x.

[28] Huang J, Yang X, Shi D, Yu H, Dong C, Hu X. Systematic methodology for high temperature LCF life prediction of smooth and notched Ni-based superalloy with and without dwells. Comput Mater Sci 2014;89:65–74. http://dx.doi.org/10.1016/j.commatsci.2014.03.023.

[29] Reis L, Li B, De Freitas M. A multiaxial fatigue approach to rolling contact fatigue in railways. Int J Fatigue 2014;67:191–202. http://dx.doi.org/10.1016/j.ijfatigue.2014.02.001.

[30] Cruces AS, Lopez-Crespo P, Moreno B, Antunes FV. Multiaxial fatigue life prediction on S355 structural and offshore steel using the SKS critical plane model. Metals 2018;8(12):1060. http://dx.doi.org/10.3390/met8121060.

[31] El-sayed HM, Lotfy M, El-din Zohny HN, Riad HS. Prediction of fatigue crack initiation life in railheads using finite element analysis. Ain Shams Eng J 2018;9(4):2329–42. http://dx.doi.org/10.1016/j.asej.2017.06.003.

[32] Zhu SP, Yu ZY, Correia J, De Jesus A, Berto F. Evaluation and comparison of critical plane criteria for multiaxial fatigue analysis of ductile and brittle materials. Int J Fatigue 2018;112:279–88. http://dx.doi.org/10.1016/j.ijfatigue.2018.03.028.

[33] Liao D, Zhu SP, Qian G. Multiaxial fatigue analysis of notched components using combined critical plane and critical distance approach. Int J Mech Sci 2019;160:38–50. http://dx.doi.org/10.1016/j.ijmecsci.2019.06.027.

[34] Cruces AS, Garcia-Gonzalez A, Moreno B, Itoh T, Lopez-Crespo P. Critical plane based method for multiaxial fatigue analysis of 316 stainless steel. Theor Appl Fract Mech 2022;118:103273. http://dx.doi.org/10.1016/j.tafmec.2022.103273.

[35] Wang J, Liu J, Hua F, He Y, Wang X. Critical plane-based fatigue life model under multiaxial random loading. Int J Struct Integr 2022;13(5):845–56. http://dx.doi.org/10.1108/IJSI-06-2022-0083.

[36] Taylor DS, Pan J. Fatigue crack initiation in threaded fasteners using the critical plane approach. In: SAE technical papers, vol. 112. 2003, p. 318–25. http://dx.doi.org/10.4271/2003-01-0697.

[37] Karolczuk A, Macha E. A review of critical plane orientations in multiaxial fatigue failure criteria of metallic materials. Int J Fract 2005;134(3–4):267–304. http://dx.doi.org/10.1007/s10704-005-1088-2.

[38] Hemmesi K, Farajian M, Fatemi A. Application of the critical plane approach to the torsional fatigue assessment of welds considering the effect of residual stresses. Int J Fatigue 2017;101:271–81. http://dx.doi.org/10.1016/j.ijfatigue.2017.01.023.

[39] Hu C, Wei D, Wang Y, Jiang X. Introduction of fretting-contact-induced crack closure: Numerical simulation of crack initiation and growth path in disk/blade attachment. Chin J Aeronaut 2019;32(8):1923–32. http://dx.doi.org/10.1016/j.cja.2019.04.011.

[40] Jiang Y, Feng M. Modeling of fatigue crack propagation. J Eng Mater Technol 2004;126(1):77–86. http://dx.doi.org/10.1115/1.1631026.

[41] Mei X, Ge S, Zheng Y. Research of fatigue crack growth based on critical plane method. In: MATEC web of conferences, vol. 67. EDP Sciences; 2016, p. 03020. http://dx.doi.org/10.1051/matecconf/20166703020.

[42] Wang D, Tan B, Xiang S, Wang X. Fatigue crack propagation and life analysis of stud connectors in steel-concrete composite structures. Sustainability (Switzerland) 2022;14(12):7253. http://dx.doi.org/10.3390/su14127253.

[43] Marques JME, Benasciutti D, Carpinteri A, Spagnoli A. An algorithm for fast critical plane search in computer-aided engineering durability analysis under multiaxial random loadings: Application to the Carpinteri–Spagnoli–Vantadori spectral method. Fatigue Fract Eng Mater Struct 2020;43(9):1978–93. http://dx.doi.org/10.1111/ffe.13273.

[44] Marulo G, Frendo F, Bertini L, Fatemi A. On the application of a critical plane approach to the life assessment of welded joints. Procedia Eng 2018;213:448–58. http://dx.doi.org/10.1016/J.PROENG.2018.02.044.

[45] Concli F, Maccioni L. Critical planes criteria applied to gear teeth: Which one is the most appropriate to characterize crack propagation? In: WIT transactions on engineering sciences, vol. 133. 2021, p. 15–25. http://dx.doi.org/10.2495/MC210021.

[46] Behrooz. Critical plane fatigue damage analysis of a high speed microgenerator shaft. 2008, p. 1206–14.

[47] Arora P, Gupta SK, Samal MK, Chattopadhyay J. Multiaxial fatigue tests under variable strain paths and asynchronous loading and assessment of fatigue life using critical plane models. Int J Fatigue 2021;145:106049. http://dx.doi.org/10.1016/j.ijfatigue.2020.106049.

[48] Ran Y, Liu J, Xie L. Multiaxial fatigue life prediction method considering notch effect and non-proportional hardening. Eng Fail Anal 2022;136:106202. http://dx.doi.org/10.1016/j.engfailanal.2022.106202.

[49] Ran Y, Liu J, Wei Y. Probabilistic fatigue framework of notched specimens based on modified strain energy density model under multiaxial loadings. Eng Fract Mech 2022;266:108401. http://dx.doi.org/10.1016/j.engfracmech.2022.108401.

[50] Wentingmann M, Noever-Castelos P, Balzani C. An adaptive algorithm to accelerate the critical plane identification for multiaxial fatigue criteria. In: Proceedings of the 6th European conference on computational mechanics: solids, structures and coupled problems, ECCM 2018 and 7th European conference on computational fluid dynamics. ECFD 2018, 2020, p. 3745–54.

[51] Sunde SL, Berto F, Haugen B. Efficient implementation of critical plane for 3D stress histories using triangular elements. Int J Fatigue 2020;134:105448. http://dx.doi.org/10.1016/j.ijfatigue.2019.105448.

[52] Liu J, Ran Y, Wei Y, Zhang Z. A critical plane-based multiaxial fatigue life prediction method considering the material sensitivity and the shear stress. Int J Press Vessels Pip 2021;194:104532. http://dx.doi.org/10.1016/j.ijpvp.2021.104532.

[53] Albinmousa J, Al Hussain M. Polar damage sum concept for constant amplitude proportional and nonproportional multiaxial fatigue analysis. Forces Mech 2021;4:100025. http://dx.doi.org/10.1016/j.finmec.2021.100025.

[54] Ma T-H, Zhou C-Y, Gao N, Chang L, He X-H. Low cycle fatigue behavior of CP-Ti under multiaxial load-controlled mode at different multiaxial stress ratios. Int J Fatigue 2022;160:106868. http://dx.doi.org/10.1016/j.ijfatigue.2022.106868.

[55] Fatemi A, Kurath P. Multiaxial fatigue life predictions under the influence of mean-stresses. J Eng Mater Technol Trans ASME 1988;110(4):380–8. http://dx.doi.org/10.1115/1.3226066.

[56] Jiang Y, Hertel O, Vormwald M. An experimental evaluation of three critical plane multiaxial fatigue criteria. Int J Fatigue 2007;29(8):1490–502. http://dx.doi.org/10.1016/j.ijfatigue.2006.10.028.

[57] Findley WN. A theory for the effect of mean stress on fatigue of metals under combined torsion and axial load or bending. J Eng Ind 1959;81(4):301–5. http://dx.doi.org/10.1115/1.4008327.

[58] Chen X, Xu S, Huang D. Critical plane-strain energy density criterion for multiaxial low-cycle fatigue life under non-proportional loading. Fatigue Fract Eng Mater Struct 1999;22(8):679–86. http://dx.doi.org/10.1046/j.1460-2695.1999.00199.x.

[59] Liu KC, Wang JA. An energy method for predicting fatigue life, crack orientation, and crack growth under multiaxial loading conditions. Int J Fatigue 2001;23(SUPPL. 1):129–34. http://dx.doi.org/10.1016/s0142-1123(01)00169-4.

[60] De Jesus VL, Pérez CA, De Oliveira AL, Sasaki DG. Understanding the gyroscope sensor: A quick guide to teaching rotation movements using a smartphone. Phys Educ 2019;54(1):015003. http://dx.doi.org/10.1088/1361-6552/aae3fc.

[61] Chiocca A, Frendo F, Bertini L. Evaluation of heat sources for the simulation of the temperature distribution in gas metal arc welded joints. Metals 2019;9(11):1142. http://dx.doi.org/10.3390/met9111142.

[62] Chiocca A, Frendo F, Bertini L. Experimental evaluation of relaxed strains in a pipe-to-plate welded joint by means of incremental cutting process. Proc Struct Integr 2020;28:2157–67. http://dx.doi.org/10.1016/j.prostr.2020.11.043.

[63] Chiocca A, Frendo F, Aiello F, Bertini L. Influence of residual stresses on the fatigue life of welded joints. Numerical simulation and experimental tests. Int J Fatigue 2022;162:106901. http://dx.doi.org/10.1016/j.ijfatigue.2022.106901.

[64] Chiocca A. Influence of residual stresses on the fatigue life of welded joints (Ph.D. thesis), University of Pisa; 2021, p. 97. http://dx.doi.org/10.13131/unipi/etd/10252021-122902.

[65] Tsavdaridis KD, D'Mello C. Optimisation of novel elliptically-based web opening shapes of perforated steel beams. J Construct Steel Res 2012;76:39–53. http://dx.doi.org/10.1016/j.jcsr.2012.03.026.

[66] Lopez Z, Fatemi A. A method of predicting cyclic stress-strain curve from tensile properties for steels. Mater Sci Eng A 2012;556:540–50. http://dx.doi.org/10.1016/j.msea.2012.07.024.

[67] Wang CH, Brown MW. Life prediction techniques for variable amplitude multiaxial fatigue—Part 1: Theories. J Eng Mater Technol Trans ASME 1996;118(3):367–70. http://dx.doi.org/10.1115/1.2806821.

[68] Wang CH, Brown MW. Life prediction techniques for variable amplitude multiaxial fatigue—Part 2: Comparison with experimental results. J Eng Mater Technol Trans ASME 1996;118(3):371–4. http://dx.doi.org/10.1115/1.2806822.

[69] Janssens KG. Universal cycle counting for non-proportional and random fatigue loading. Int J Fatigue 2020;133:105409. http://dx.doi.org/10.1016/j.ijfatigue.2019.105409.

[70] Bannantine JA, Socie DF. A variable amplitude multiaxial fatigue life prediction method. In: Third international conference on biaxial/multiaxial fatigue. 1989, p. 12.1 – 12.20.

[71] Zhu SP, Yu ZY, Correia J, De Jesus A, Berto F. Evaluation and comparison of critical plane criteria for multiaxial fatigue analysis of ductile and brittle materials. Int J Fatigue 2018;112:279–88. http://dx.doi.org/10.1016/j.ijfatigue.2018.03.028.

[72] Skibicki D, Pejkowski Ł. Low-cycle multiaxial fatigue behaviour and fatigue life prediction for CuZn37 brass using the stress-strain models. Int J Fatigue 2017;102:18–36. http://dx.doi.org/10.1016/j.ijfatigue.2017.04.011.

[73] Zhu SP, Liu Q, Zhou J, Yu ZY. Fatigue reliability assessment of turbine discs under multi-source uncertainties. Fatigue Fract Eng Mater Struct 2018;41(6):1291–305. http://dx.doi.org/10.1111/ffe.12772.